

A Highly Crystalline Manganese-Doped Iron Oxide Nanocontainer with Predesigned Void Volume and Shape for Theranostic Applications

Vu Ngoc Phan, Eun-Kyung Lim, Taekhoon Kim, Minsik Kim, Yuna Choi, Byeongyoon Kim, Myounghoon Lee, Aram Oh, Juhong Jin, Youngjoo Chae, Hionsuck Baik, Jin-Suck Suh, Seungjoo Haam, Yong-Min Huh,* and Kwangyeol Lee*

Theranostics has been introduced for monitoring the therapeutic response of a tumor to anti-proliferative chemotherapeutic agents, and a number of nanoparticle-based theranostic systems have been developed.^[1–19] The major challenge in successful clinical translation of nanoparticle-based drug delivery lies in demonstrating significantly enhanced therapeutic efficacy over the current clinical therapies. Therefore, theranostic nanoparticles that are capable of simultaneous non-invasive diagnosis and treatment of disease need to be designed to deliver a therapeutic cargo to a tumor efficiently and in a target-specific fashion. This would greatly enhance the safety and efficacy of cancer treatment by minimizing the amount of diagnostic nanocontainers employed and thereby reducing nanomaterial-related toxicity. In order to maximize drug-loading efficiency, hollow inorganic nanocontainers with the ability to enhance image contrast enhancement have been developed as theranostic nanoplatfroms.^[15–24] The drug-loading efficiency of nanocontainers is determined by the physical dimensions and morphology of the cavity, as well as the nature of the drug-cavity interaction. For effective encapsulation of

hydrophobic anticancer drugs, fine control of the void size and surface hydrophobicity, as well as nanocontainer shape, is highly desirable. However, controlling these features for theranostic nanocontainers has proved very difficult. Here, we report a novel one-pot synthetic process involving shape- and size-controlled nanoparticles as removable template cores to form hollow nanocontainers having hydrophobic cavities with predetermined shape and size. We generated hollow manganese (Mn)-doped iron oxide nanocontainers by forming an epitaxial layer of iron oxide on MnO nanoparticles and removing the MnO phase, which is destabilized by the presence of oleic acid at high temperatures. Iron oxide was chosen because of its utility as a T_2 contrast agent for magnetic resonance imaging (MRI).^[25] Depending on the initial shape of the MnO template nanoparticles, hollow Mn-doped iron oxide nanocontainers can take nanourchin, nanooctahedron, or nanocube shapes. The resulting Mn-doped iron oxide nanocontainers single-handedly help accomplish two goals: delivering an effective dose of the desired anticancer drug to tumor tissue and monitoring the fate of nanocontainers through T_2 -weighted MRI. This enabled us to achieve the optimal balance between diagnostic and therapeutic moieties in an all-in-one theranostic nanoplatfrom.

The overall synthetic process for the Mn-doped iron oxide nanocontainer is shown in **Figure 1**. Shape-controlled MnO nanoparticles were obtained from thermal decomposition of Mn precursors in the presence of oleic acid and oleylamine. These MnO nanoparticles were briefly exposed to air to form a thin Mn_3O_4 layer and then coated with an iron oxide phase, formed from decomposition of iron acetylacetonate ($Fe(acac)_3$). During this process, the Mn within the Mn_3O_4 phase diffuses out to the newly formed iron oxide shell. The resulting Mn-doped iron oxide-coated MnO nanoparticles were subjected to etching by excess oleic acid to form hollow Mn-doped iron-oxide nanocontainers.

The presence of the Mn_3O_4 layer on the surface of MnO was found to be crucial in rendering the Mn-doped iron oxide shell porous. When the prepared MnO nanoparticles were directly coated with an iron oxide layer from decomposition of iron acetylacetonate under argon, a hermetic iron oxide (Fe_3O_4) shell resulted, which did not permit the access of oleic acid to etch out the MnO core. In the presence of oxygen, the surface of MnO nanoparticles is converted to a Mn_3O_4 phase. This oxidation is not homogeneous, leading to formation of multiple domains of Mn_3O_4 on the surface of MnO nanoparticles,

Dr. V. N. Phan,^{[+], [++]} Dr. T. Kim,^[+] Dr. M. Kim, B. Kim, A. Oh, J. Jin, Y. Chae, Prof. K. Lee
Department of Chemistry and Research Institute
for Natural Sciences
Korea University
Seoul 136-701, Korea
E-mail: kylee1@ko.rea.ac.kr



Dr. E.-K. Lim,^[+] Y. Choi, M. Lee, Prof. J.-S. Suh, Prof. Y.-M. Huh
Department of Radiology
College of Medicine
Yonsei University
Seoul 120-752, Korea
E-mail: ymhuh@yuhs.ac

Dr. H. Baik
Korea Basic Science Institute (KBSI)
Seoul 136-713, Korea
Prof. S. Haam
Department of Chemical & Biomolecular Engineering
Yonsei University
Seoul 120-749, Korea

^[+] Present address: Advanced Institute for Science and Technology,
Hanoi University of Science and Technology, Hanoi, Vietnam

^[++] These authors contributed equally to this work.

DOI:10. 1002/adma.201300525

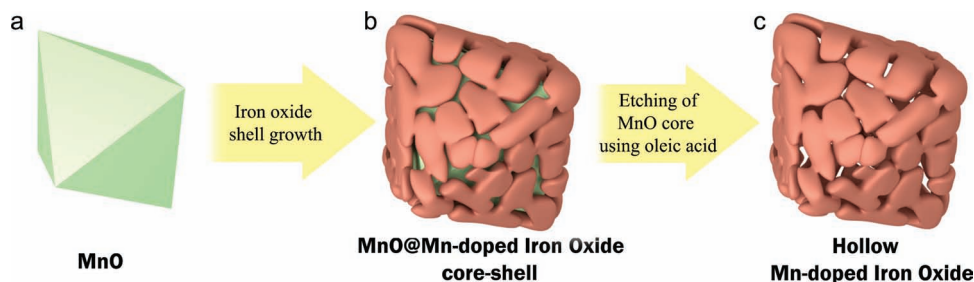


Figure 1. Schematic illustration of procedure for fabricating the hollow Mn-doped iron oxide nanocontainers: a) MnO nanoparticle, b) core-shell MnO@Mn-doped iron oxide ($\text{MnO} @ (\text{Mn}_{0.2}\text{Fe}_{0.8})_3\text{O}_4$) nanoparticle, and c) hollow Mn-doped iron oxide nanocontainer.

as demonstrated by the formation of urchin-shaped MnO nanocrystals by etching.^[25] We found that Mn_3O_4 readily mixed with the newly formed Fe_3O_4 phase to form a $(\text{Mn},\text{Fe})_3\text{O}_4$ phase (Figure S3,S4, Supporting information). Hollow Mn-doped iron oxide structures could therefore be obtained by reaction of Mn_3O_4 nanoparticles with an iron precursor through Kirkendall effect. Consistent with this finding, the growth of an iron oxide shell on the patchy Mn_3O_4 surface of the MnO core resulted in the formation of a Mn-doped iron oxide phase. Subsequently, MnO cores were removed by adding additional oleic acid to the reaction mixture and heating at 240 °C for 30 min. This resulted in the formation of monodisperse hollow nanocontainers as shown in Figure 2a. In addition to oleic acids, other long chain organic acids with high boiling points such as palmitic acid and stearic acid could be also employed for etching of MnO phase. There are a few other published examples of metal oxide destabilization by organic acids at elevated temperatures.^[25,26]

Electron energy loss spectroscopy (EELS) analysis of the hollow nanocontainers formed in this way indicated both the porous nature of the shell and the complete mixing of Mn and Fe ions in the shell (Figure 2b). Despite the patchy nature of the shell, the Mn-doped iron oxide shell is highly crystalline, as shown in the high-resolution transmission electron microscopy (HRTEM) (Figure 2c), indicating that the iron-based shell formed epitaxially on the single crystalline MnO nanoparticle substrate. The hollow nanocontainer composition was identified as $(\text{Mn}_{0.2}\text{Fe}_{0.8})_3\text{O}_4$ by energy-dispersive X-ray spectroscopy (EDAX) analysis (Figure S5,S6, Supporting information). It was previously shown that the enthalpy of formation of $(\text{Mn}_x\text{Fe}_{1-x})_3\text{O}_4$ ($x = 0$ to $x = 0.67$) from Mn_3O_4 and Fe_3O_4 is negative at 298 K, with the minimum enthalpy value near $x = 0.2$.^[27] The XPS analysis indicated that both Mn^{2+} and Mn^{3+} ions were present, implying that the Mn and iron atoms randomly occupied the divalent sites in the spinel structure (Figure S10, Supporting information). The cavity shape within the hollow Mn-doped iron oxide nanocontainers was an exact copy of the template MnO nanoparticle (Figure 2a–c). Nanourchin, nanocross, and nanocube cavity shapes could be obtained, as shown in Figure 2d–f, demonstrating the versatility of template synthesis involving facet-controlled nanoparticles. The hollow nanocontainers obtained were dispersible in organic solvents, greatly simplifying hydrophobic drug loading into the hollow void. In particular, they could be conveniently loaded with doxorubicin (DOX) by using the incipient wetness technique, whereby DOX and triethylamine dissolved in chloroform were

introduced into the void and solvent was then removed to accumulate DOX inside the hollow nanocontainers.

The formation of hollow structures can follow two general routes. The wall of a template with dimension-controlled cavities, such as AAO or mesoporous silica, can be partially deposited with a desired material before removing the template to release hollow nanostructures.^[28,29] However, there are not many available templates with the desired pore dimensions and morphologies. The second route involves the usage of removable cores. A thin porous shell is formed on a core with a different chemical composition, which is then selectively removed to leave the shell.^[7,13,16,30–39] Galvanic replacement has been a preferred method for the latter route.^[34,40–43] However, neither conformal shell formation to preserve the core and therefore cavity morphology, nor hydrophobic cavity formation, is feasible with Galvanic replacement.

It is greatly advantageous to design drug delivery vehicles to discharge their therapeutic contents only at low pH values, because tumors typically exhibit lower extracellular pH than normal tissues because of anaerobic glucose metabolism. Therefore, DOX-loaded hollow Mn-doped iron oxide nanocontainers were encapsulated with α -pyrenyl- ω -carboxyl poly(ethylene glycol) (Py-PEG-COOH or pyrenyl PEG) by a nanoprecipitation method. We have previously demonstrated the pH-dependent drug discharging behavior of pyrenyl-functionalized polymer.^[10] These pH-activatable DOX-loaded nanocontainers (NCs) exhibited a narrow size distribution of 112.6 ± 6.6 nm in an aqueous medium. They also showed a magnetization saturation value of 46.1 emu/g_{Fe+Mn} at 1.2 T with a super-paramagnetic behavior (Figure S12, Supporting information). Furthermore, their relaxivity coefficient was $119 \text{ mM}^{-1} \text{ s}^{-1}$ as measured by 1.5 T MRI, indicating a sufficiently high sensitivity as an MRI contrast agent (Figure S12, Supporting information). Some of us previously reported that non-hollow Mn-doped iron oxide magnetic nanoparticles could be designed to exhibit a stronger MR contrast effect with a relaxivity value of $358 \text{ mM}^{-1} \text{ s}^{-1}$ and a high mass magnetization value ($110 \text{ emu/g}_{\text{Fe+Mn}}$).^[9] Although the hollow nanocontainer developed in our work does not reach the MR contrast ability of non-hollow Mn-doped iron oxide nanoparticles, the ability to load hydrophobic drugs is not attainable by non-hollow magnetic nanoparticles. There have been attempts to co-encapsulate non-hollow magnetic nanoparticles and hydrophobic drugs by amphiphilic polymers,^[8,10] but the loading efficiency of these systems is much inferior to that of the hollow nanocontainer developed in our work.

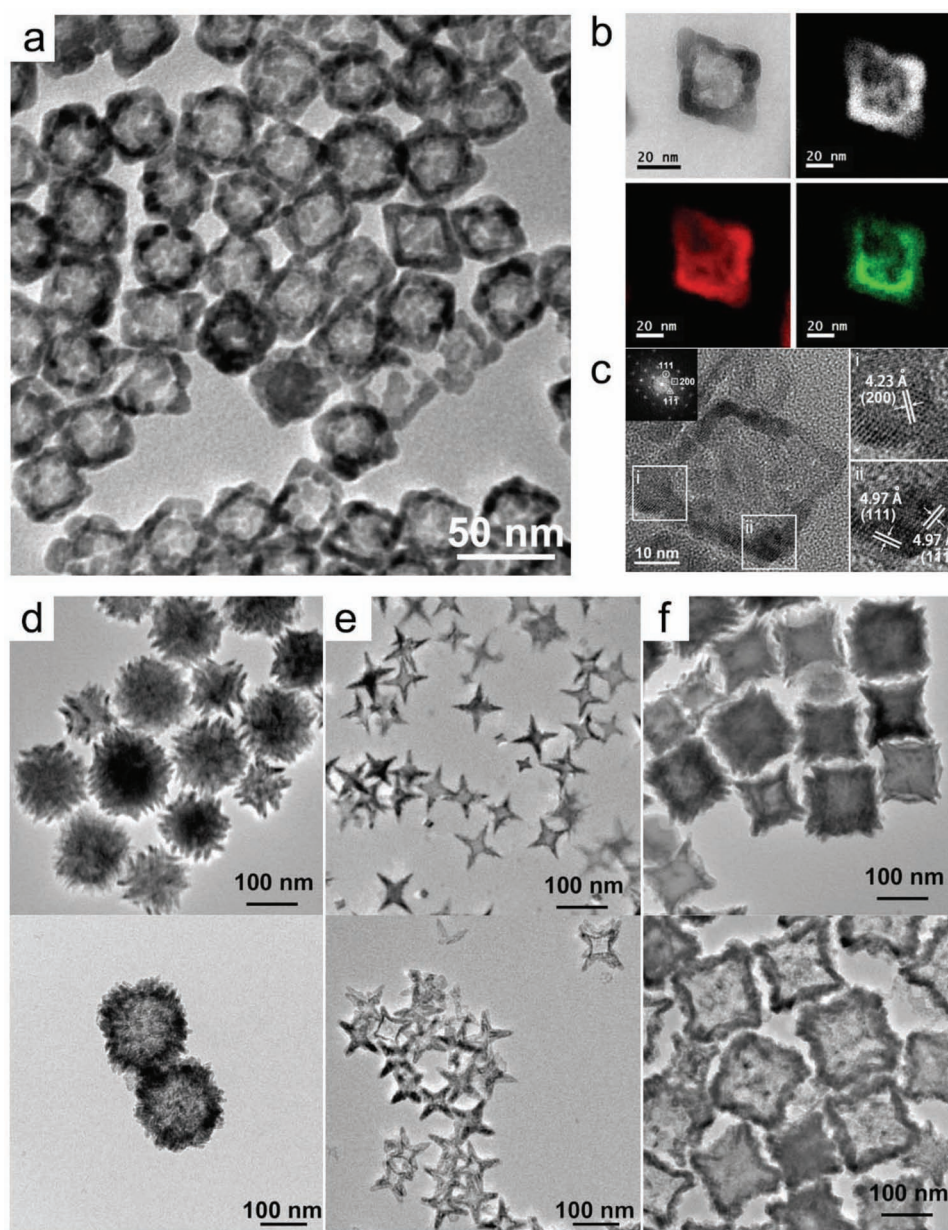


Figure 2. a) A TEM image of hollow Mn-doped iron oxide nanoparticles. b) EELS analysis showing the elemental mapping images for oxygen (white), iron (red) and manganese (green). c) An HRTEM image showing its crystallinity. TEM images of (upper) $\text{MnO}@\text{Mn}_{0.2}\text{Fe}_{0.8}\text{O}_4$ nanoparticles and (lower) hollow Mn-doped iron oxide nanoparticles (d: urchin-shape, e: cross-shape f: cubic-shape) obtained from them.

The drug release behavior of the NCs was examined under various pH conditions at 37 °C. As expected, NCs showed a distinct pH-dependent drug release profile (Figure 3a). DOX was released quickly from NCs at pH 5.5 because π - π interactions between DOX and pyrene groups were weakened by the proton rich environment, and therefore, the solubility of protonated DOX in the aqueous solution was increased, as compared to pH 7.4 and 9.8.^[44] At all three pH conditions, the DOX-NCs showed an initial burst of DOX release (phase I: initial 1 h) with release kinetics constants (k) of 8.3, 3.79 and 1.27 at pH 5.5, 7.4, and 9.8 respectively. This resulted in the release of 20, 11.9,

and 4.4% of the DOX cargo, respectively. However, after this initial burst, DOX release was more sustained at a high pH, with 24.6% released over 5 h (0.05–0.21 day; phase II) at pH 7.4 ($k = 0.33$), and 8.4% at pH 9.8 ($k = 0.20$). The present study indicated that nearly 30 or 80% of the DOX cargo remained entrapped in the NCs for 7 d at pH 7.4 and pH 9.8, respectively. However, nearly 66% of DOX was released within 5.5 h at pH 5.5 (Figure 3b and Figure S13, Supporting information). These results indicated that NCs minimized drug leakage during blood circulation (pH 7.4) prior to reaching the target cancer cells, where the drug release rate would be accelerated.^[45–47]

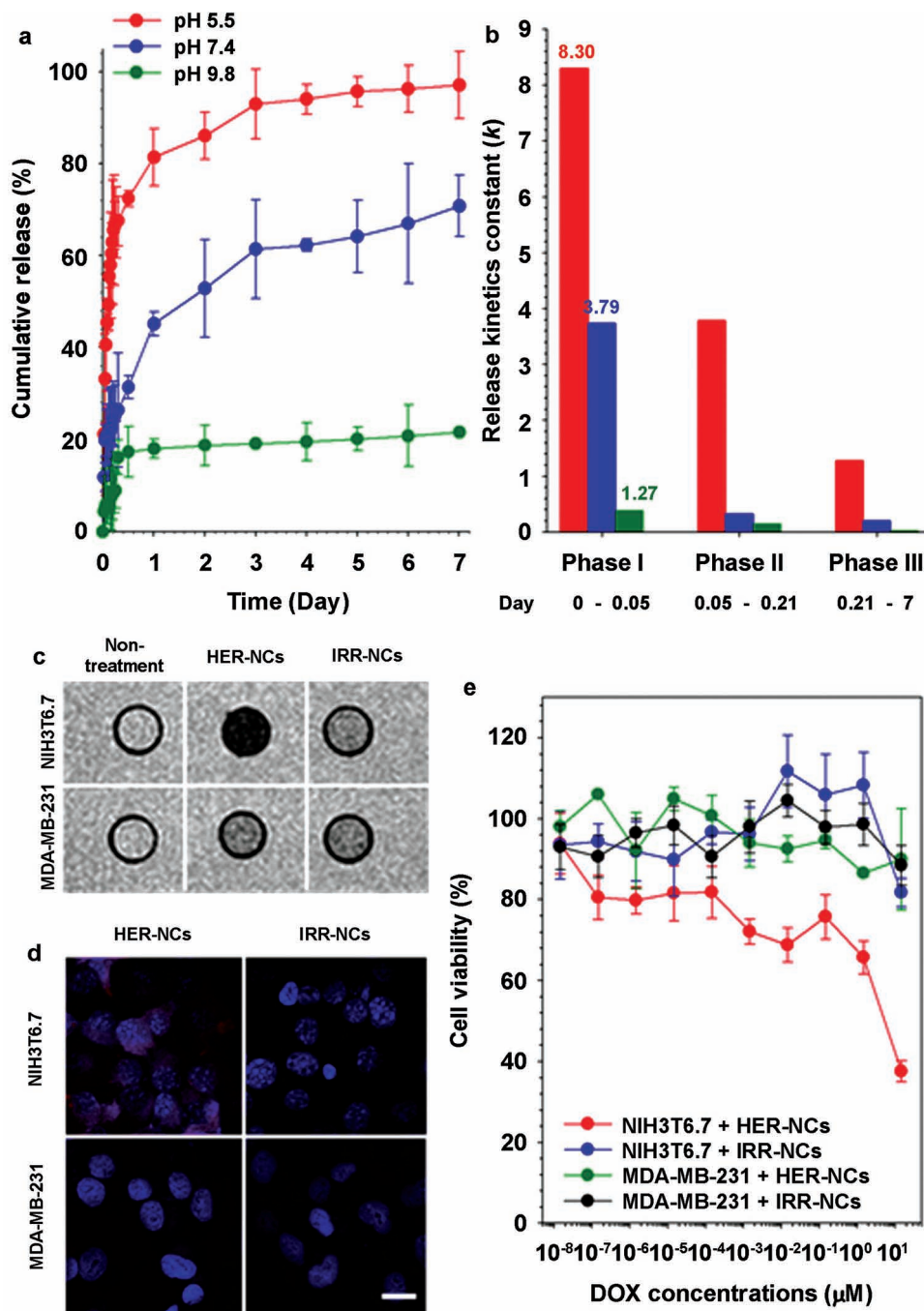


Figure 3. a) pH-sensitive drug release profiles of NCs for 7 d (red: pH 5.5; blue: pH 7.4; green: pH 9.8). b) Graph of drug release kinetic constants (k) versus the various phases (I: 0 - 0.05 day, II: 0.05–0.21 day and III: 0.21–7 day) at various pH conditions (* p and ** p < 0.001). c,d) T_2 -weighted MR images (c) and fluorescence images (d) of target cells (NIH3T6.7 and MDA-MB-231) incubated with HER-NCs and IRR-NCs, respectively: The red fluorescence indicates doxorubicin. Blue indicates cellular nuclei stained with Hoechst 33342 (scale bar: 20 μm). e) Cell viability test of target cells treated with HER-NCs and IRR-NCs, respectively.

The pH-induced drug release concept has been also demonstrated with non-magnetic inorganic core-shell structures (e.g., CaCO_3 and NaHCO_3).^[48–50] However, it should be noted that these nanostructures discharge loaded drugs concomitant with the structural disintegration of nanostructures under acidic condition, while the change in the π - π interaction between

drug and pyrene groups has been exploited for acidic condition-induced drug release in our work.

The pyrenyl-PEG-modified NCs were further modified by anti-HER2/neu antibody (Herceptin: HER) for synergistic cancer therapy by receptor-mediated endocytosis.^[13] The therapeutic efficacy of NCs modified with anti-HER2/neu antibody

(HER-NCs) was compared with those modified using an irrelevant antibody, (IgG)-modified NCs (IRR-NCs). We investigated the targeting ability of HER-NCs using MRI and flow cytometry analysis in relevant cell lines; NIH3T6.7 (HER2/neu receptor overexpressing cells) and MDA-MB-231 (HER2/neu receptor underexpressing cells). HER-NC-treated NIH3T6.7 cells appeared very dark on MRI, while HER-NC-treated MDA-MB-231 cells showed no significant difference when compared with non-treated cells (Figure 3c). This indicated that HER-NCs were interacting with HER2/neu receptors. The target specificity of HER-NCs toward NIH3T6.7 cells was also confirmed by its fluorescence intensity values (90.8%), which were significantly higher than other conditions (Figure S14a,b, Supporting information). The MR signal intensity ratio represents the relaxivity (R_2) difference between NC-treated cells and non-treated cells (Non-treatment) ($\Delta R_2/R_{2, \text{Non-treatment}}$, where $\Delta R_2 = R_2 - R_{2, \text{Non-treatment}}$ and $R_2 = T_2^{-1}$). HER-NC-treated NIH3T6.7 cells exhibited much stronger signal enhancement with 234.5%, as compared with others (HER-NC-treated MDA-MB-231 cells: 25.0%, IRR-NC-treated NIH3T6.7 cells: 4.5% and IRR-NC-treated MDA-MB-231 cells: 9.6%) (Figure 3c and Figure S14, Supporting information).

We then investigated the NC drug release behavior with specific cancer cells by incubating HER-NC or IRR-NC with NIH3T6.7 and MDA-MB-231 cells, respectively (Figure 3d and Figure S15, Supporting information). Internalization of DOX into cells was easily identified using fluorescence images because DOX emits a red fluorescence signal. Consistent with the cell targeting experiments, HER-NCs were specifically delivered to NIH3T6.7 cells by receptor-mediated endocytosis. Only NIH3T6.7 cells treated with HER-NC displayed a red fluorescence, indicating that DOX released from HER-NC accumulated intracellularly (cytoplasm and nucleus), whereas DOX from HER-NC did not reach the interior of MDA-MB-231 cells. In addition, IRR-NC-treated cells did not show any DOX fluorescence. We evaluated the viability of these cell lines to assess the anti-cancer activity of HER-NC. As shown in Figure 3e, HER-NC exhibited high toxicity when used to treat NIH3T6.7 cells ($IC_{50} = 1.7 \times 10^{-12}$ μM), while toxicity was hardly observed in other conditions at same DOX concentrations. This is consistent with the proposal that the DOX internalized from HER-NC initiated the cell death pathway within NIH3T6.7 cells.

Finally, we monitored intra-tumoral distribution of HER-NCs using in vivo temporal MR imaging after intravenous

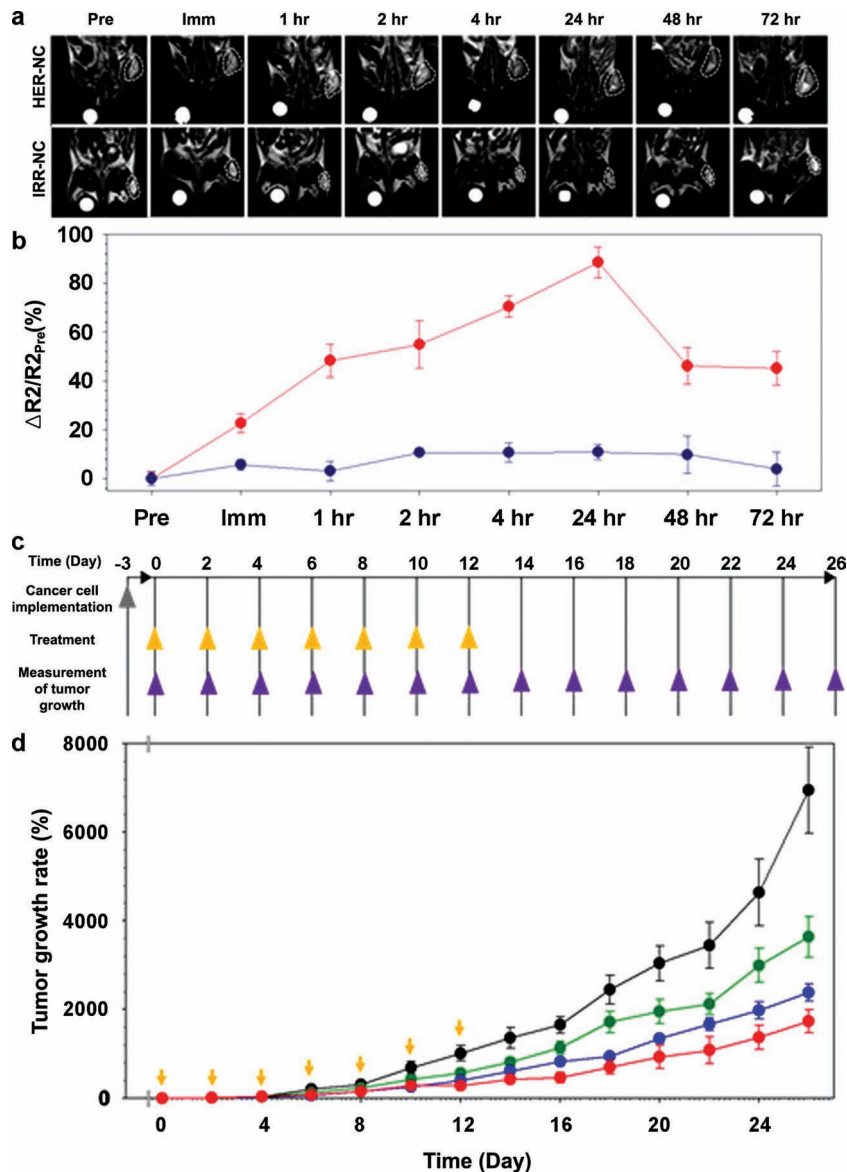


Figure 4. a) T_2 -weighted MR images of cancer targeting events of HER-NCs (upper) and IRR-NCs (lower) in NIH3T6.7 cells implanted in xenograft mice at various time intervals. Tumor regions are indicated by white dashed lines. b) $\Delta R_2/R_{2, \text{Pre}}$ graph versus time after injections of HER-NCs and IRR-NCs, respectively (red circles: HER-NCs and blue circles: IRR-NCs). c) The therapeutic dosing schedule of each therapeutic condition (HER-NCs, IRR-NCs, Doxorubicin and saline) (yellow triangles) and measurement of tumor growth (purple triangles). d) Comparative therapeutic efficacy study in the in vivo model. (red circles: HER-NCs, blue circles: IRR-NCs, green circles: DOX and black circles: saline).

injection into tumor-bearing mice (57.2 μg of Fe+Mn, 3 mg of DOX) (Figure 4a,b). As soon as HER-NCs were administrated (Immediately: Imm), tumor sites were darkened with a high MR signal intensity, which had increased by 22.6% compared with pre-injection (Pre). The MR signals at the tumor sites gradually became stronger over time, reaching the maximal MR signal (88.6%) at 24 h post-injection. This indicated that HER-NCs effectively accumulated at tumor sites, as evidenced by the significant enhancement of MR signal. After 24 h after injection, HER-NCs were gradually secreted from the mouse

body. In mice injected with IRR-NC, the tumor site was also slightly darkened immediately after injection (Imm) with 5.7% of MR signal, due to non-specific binding.^[51]

Using the drug release profiling and in vivo MRI studies, we determined the therapeutic dosing schedule of HER-NC for effective cancer therapy. HER-NC concentration was maximal at the tumor site 24 h post injection and over 80% of the DOX cargo was released within 24 h in the acidic environment. Therefore, we administrated HER-NC every 48 h to ensure that tumor drug concentration was consistently maintained for an effective cancer therapy. HER-NC, IRR-NC, free DOX and saline were administrated to four individual subgroups of tumor-bearing mice ($n = 10$) via intravenous (I.V.) injection. After the mouse tumor volume reached approximately 40 mm³, each treatment was administrated every 2 d (48 h) for 12 d (injections on days 0, 2, 4, 6, 8, 10 and 12). After completion of the drug administration schedule, tumor sizes within each treatment group were further monitored every 2 d for 26 d (Figure 4c).

HER-NC was significantly more efficacious at tumor growth inhibition when compared with the control (saline), DOX, and IRR-NC groups. After administration for 12 d, the tumor volume growth was remarkably suppressed in the HER-NC-treated group, confirming that its cancer-specific targeting ability had an important role in improving therapeutic efficacy. After ending the drug administration at day 12, we monitored tumor growth for 14 additional days. At day 26, an average tumor growth of 1732.6% was observed for the HER-NC-treated group. Saline and DOX-treated groups showed a continuous tumor growth (saline: 6945.6% and DOX: 3636.2%) (Figure 4c). On the other hand, a slightly reduced tumor growth of 2379.1% was observed for IRR-NC-treated mice, perhaps reflecting the non-specific accumulation of IRR-NC at the tumor site by an enhanced permeability and retention effect (EPR) (Figure 4d).^[9,10,52–56]

Therefore, although administration of HER-NC could not completely suppress tumor growth after cessation of drug administration, its tumor-growth-suppression performance was far superior to that of saline, DOX, and IRR-NC (Figure S16, Supporting information). It should be noted that anti-proliferative chemotherapeutic agents such as DOX have shown limited success for the treatment of solid tumors due to drug resistance and therefore overdosing does not lead to complete tumor regression.^[52,57,58] Furthermore, the theranostic nanocontainers developed in this study could provide valuable information about therapeutic response and optimal drug administration schedules.

In summary, we have developed a new route to the production of theranostic hollow nanocontainers with a hydrophobic cavity and predesigned cavity shape and size. The process consists of formation of a porous shell on shape-controlled nanoparticles, followed by removal of the core under nanoparticle-destabilizing conditions. The resulting Mn-doped iron oxide nanocontainers successfully delivered and discharged an effective dose of an anticancer drug to tumor tissue in a pH-dependent manner, and facilitated monitoring of the fate of the nanocontainers using T_2 -weighted MRI. The drug administration schedule and therapeutic tumor response could be optimized using the drug release profile, as well as

the data on the drug container residing time in the tumor. The optimal balance between diagnostic and therapeutic moieties in this all-in-one theranostic nanoplatform would be crucial for clinical translation of nanoparticle-based therapy. We expect that the nanoparticle-templating strategy described here can be further exploited for the preparation of other useful hollow nanostructures with predesigned cavity size and shape and also that the efficacy and drug administration schedule of other therapeutic contents can be tested using these novel theranostic nanocontainers.

Experimental Section

Preparation of Hollow Mn-Doped Iron Oxide Nanocontainers: MnO nanoparticles and iron(III) acetylacetonate were added into a solution of oleic acid (0.05 mmol), oleylamine (1 mmol), and trioctylamine (2 mL) in a 100 mL Schlenk tube. The Schlenk tube was heated in the oil bath to 210 °C with the heating rate of 10 °C per min under vigorous magnetic stirring and kept at this temperature for 20 min under argon. The reaction mixture was then heated at 310 °C for 30 min under a dry air environment (20% oxygen). The black solution was cooled to room temperature, and a solution of oleic acid (1.3 mmol) and trioctylamine (0.5 mL) was added to it. The reaction mixture was heated to 240 °C and kept at this temperature for 30 min under a dry air environment. After cooling to room temperature, the hollow Mn-doped iron oxide nanocrystals were precipitated with an addition of acetone and n-propanol and were collected by centrifugation (3 min, 3500 rpm). The obtained nanoparticles were washed several times in hexane and ethanol. The nanoparticles could be redispersed in chloroform, hexane, or toluene for further usage.

Drug Loading of Hollow Mn-Doped Iron Oxide Nanocontainers: DOX was loaded into hollow Mn-doped iron oxide nanocontainers using a typical incipient wetness method. DOX and triethylamine were dissolved in chloroform (4 mL). Hollow Mn-doped iron oxide nanocontainers were dispersed in chloroform (4 mL) and added into this solution. The resultant solution was gently stirred for 10 min at room temperature before placing under vacuum to evaporate the solvent. The resultant red powder was dispersed in chloroform (4 mL) and the DOX-loaded nanocontainers were collected with a permanent magnet to remove unloaded free DOX. The above procedure was repeated three times to accumulate DOX in the nanocontainer.

Preparation of pH-Activatable DOX-Loaded Nanocontainers: The freshly prepared solution of DOX-loaded Mn-doped iron oxide nanocontainers in tetrahydrofuran (THF) (1 mL) was quickly injected into a buffer solution (50 mL) at pH 9.8 containing pyrenyl PEG (300 mg) to minimize unwanted drug release. The resulting suspension was stirred overnight at room temperature to evaporate the organic solvent and subsequently centrifuged for 45 min at 20 000 rpm. After the supernatant removal, the precipitated DOX-loaded pH-activatable Mn-doped iron oxide nanocontainers were redispersed in pH 7.4 buffer (10 mL).

Supporting Information

Supporting Information is available from the Wiley Online Library or from the author.

Acknowledgements

This work was supported by NRF 2010-0014807, NRF 2010-0020648, and NRF 2010-0020209, NRF 2010-0019923, MIHWAF (the Korea Health 21 R&D Project: A085136), the KRIBB Research Initiative Program, and

iNtRON biotechnology. We thank KBSI for allowing the usage of their HRTEM instrument.

Received: January 31, 2013

Revised: March 4, 2013

Published online: May 3, 2013

- [1] J. Xie, S. Lee, X. Chen, *Adv. Drug Delivery Rev.* **2010**, *62*, 1064.
- [2] S. Mura, P. Couvreur, *Adv. Drug Delivery Rev.* **2012**, *64*, 1394.
- [3] D.-E. Lee, H. Koo, I.-C. Sun, J. H. Ryu, K. Kim, I. C. Kwon, *Chem. Soc. Rev.* **2012**, *41*, 2656.
- [4] F. M. Kievit, M. Zhang, *Adv. Mater.* **2011**, *23*, H217.
- [5] M. P. Melancon, R. J. Stafford, C. Li, *J. Controlled Release* **2012**, *164*, 177.
- [6] O. C. Farokhzad, R. Langer, *ACS Nano* **2009**, *3*, 16.
- [7] C. Moorthi, R. Manavalan, K. Kathiresan, *J. Pharm. Pharmaceut. Sci.* **2011**, *14*, 67.
- [8] J. Yang, C. H. Lee, H. J. Ko, J. S. Suh, H. G. Yoon, K. Lee, Y. M. Huh, S. Haam, *Angew. Chem. Int. Ed.* **2007**, *46*, 8836.
- [9] J. H. Lee, Y. M. Huh, Y. W. Jun, J. W. Seo, J. T. Jang, H. T. Song, S. Kim, E. J. Cho, H. G. Yoon, J. S. Suh, J. Cheon, *Nat. Med.* **2007**, *13*, 95.
- [10] E. K. Lim, Y. M. Huh, J. Yang, K. Lee, J. S. Suh, S. Haam, *Adv. Mater.* **2011**, *23*, 2436.
- [11] J. Chen, M. Yang, Q. Zhang, E. C. Cho, C. M. Cobley, C. Kim, C. Glaus, L. V. Wang, M. J. Welch, Y. Xia, *Adv. Funct. Mater.* **2010**, *20*, 3684.
- [12] N. Nasongkla, E. Bey, J. Ren, H. Ai, C. Khemtong, J. S. Guthi, S.-F. Chin, A. D. Sherry, D. A. Boothman, J. Gao, *Nano Lett.* **2006**, *6*, 2427.
- [13] P. Horcajada, T. Chalati, C. Serre, B. Gillet, C. Sebrie, T. Baati, J. Eubank, D. Heurtaux, P. Clayette, C. Kreuz, J. Chang, Y. Hwang, V. Marsaud, P. Bories, L. Cynober, S. Gil, G. Férey, P. Couvreur, R. Gref, *Nat. Mater.* **2010**, *9*, 172.
- [14] J.-H. Lee, J.-T. Jang, J.-S. Choi, S. H. Moon, S.-H. Noh, J.-W. Kim, I.-S. Kim, K. I. Park, J. Cheon, *Nat. Nanotechnol.* **2011**, *6*, 418.
- [15] Y. Piao, J. Kim, H. B. Na, D. Kim, J. S. Baek, M. K. Ko, J. H. Lee, M. Shokouhimehr, T. Hyeon, *Nat. Mater.* **2008**, *7*, 242.
- [16] J. Shin, R. M. Anisur, M. K. Ko, G. H. Im, J. H. Lee, I. S. Lee, *Angew. Chem. Int. Ed.* **2009**, *48*, 321.
- [17] K. Cheng, S. Peng, C. Xu, S. Sun, *J. Am. Chem. Soc.* **2009**, *131*, 10637.
- [18] Y. Chen, H. Chen, D. Zeng, Y. Tian, F. Chen, J. Feng, J. Shi, *ACS Nano* **2010**, *4*, 6001.
- [19] M. S. Yavuz, Y. Cheng, J. Chen, C. M. Cobley, Q. Zhang, M. Rycenga, J. Xie, C. Kim, K. H. Song, A. G. Schwartz, L. V. Wang, Y. Xia, *Nat. Mater.* **2009**, *8*, 935.
- [20] Y. Lu, L. Dong, L.-C. Zhang, Y.-D. Su, S.-H. Yu, *Nano Today* **2012**, *7*, 297.
- [21] Y. Lu, Y. Zhao, L. Yu, L. Dong, C. Shi, M.-J. Hu, Y.-J. Xu, L.-P. Wen, S.-H. Yu, *Adv. Mater.* **2010**, *22*, 1407.
- [22] Y. Lu, C. Shi, M.-J. Hu, Y.-J. Xu, L. Yu, L.-P. Wen, Y. Zhao, W.-P. Xu, S.-H. Yu, *Adv. Funct. Mater.* **2010**, *20*, 3701.
- [23] Y. Zhao, Y. Lu, Y. Hu, J.-P. Li, L. Dong, L.-N. Lin, S.-H. Yu, *Small* **2010**, *6*, 2436.
- [24] Y. Lu, L. Zhang, J. Li, Y.-D. Su, Y. Liu, Y.-J. Xu, L. Dong, H.-L. Gao, J. Lin, N. Man, P.-F. Wei, W.-P. Xu, S.-H. Yu, L.-P. Wen, *Adv. Funct. Mater.* **2013**, *23*, 1534.
- [25] T. Kim, E. J. Cho, Y. Chae, M. Kim, A. Oh, J. Jin, E. S. Lee, H. Baik, S. Haam, J. S. Suh, Y. M. Huh, K. Lee, *Angew. Chem. Int. Ed.* **2011**, *50*, 10589.
- [26] S. Kim, M. Kim, T. Kim, H. Baik, K. Lee, *CrystEngComm* **2013**, *49*, 2225.
- [27] S. Guillemet-Fritsch, A. Navrotsky, P. Tailhades, H. Coradin, M. Wang, *J. Solid State Chem.* **2005**, *178*, 106.
- [28] H. HMasuda, K. Fukuda, *Science* **1995**, *268*, 1466.
- [29] J. C. Hulteen, C. R. Martin, *J. Mater. Chem.* **1997**, *7*, 1075.
- [30] D. H. Son, S. M. Hughes, Y. Yin, A. P. Alivisatos, *Science* **2004**, *306*, 1009.
- [31] F. Caruso, *Science* **1998**, *282*, 1111.
- [32] H. Jin Fan, M. Knez, R. Scholz, K. Nielsch, E. Pippel, D. Hesse, M. Zacharias, U. Gosele, *Nat. Mater.* **2006**, *5*, 627.
- [33] M. Kim, K. Sohn, H. B. Na, T. Hyeon, *Nano Lett.* **2002**, *2*, 1383.
- [34] X. W. Lou, L. A. Archer, Z. Yang, *Adv. Mater.* **2008**, *20*, 3987.
- [35] Y. Sun, B. Mayers, Y. Xia, *Adv. Mater.* **2003**, *15*, 641.
- [36] Y. Wang, L. Cai, Y. Xia, *Adv. Mater.* **2005**, *17*, 473.
- [37] K. Kamata, Y. Lu, Y. Xia, *J. Am. Chem. Soc.* **2002**, *125*, 2384.
- [38] Y. Yin, Y. Lu, B. Gates, Y. Xia, *Chem. Mater.* **2001**, *13*, 1146.
- [39] W. J. Rieter, K. M. L. Taylor, H. An, W. Lin, W. Lin, *J. Am. Chem. Soc.* **2006**, *128*, 9024.
- [40] K. An, T. Hyeon, *Nano Today* **2009**, *4*, 359.
- [41] Q. Zhang, W. Wang, J. Goebel, Y. Yin, *Nano Today* **2009**, *4*, 494.
- [42] Y. Sun, Y. Xia, *Science* **2002**, *298*, 2176.
- [43] Z. Wang, D. Luan, F. Y. Boey, X. W. Lou, *J. Am. Chem. Soc.* **2011**, *133*, 4738.
- [44] Z. Liu, X. Sun, N. Nakayama-Ratchford, H. Dai, *ACS Nano* **2007**, *1*, 50.
- [45] R. A. Gatenby, E. T. Gawlinski, A. F. Gmitro, B. Kaylor, R. J. Gillies, *Cancer Res.* **2006**, *66*, 5216.
- [46] W. Chen, F. Meng, R. Cheng, Z. Zhong, *J. Controlled Release* **2010**, *142*, 40.
- [47] J. Z. Du, X. J. Du, C. Q. Mao, J. Wang, *J. Am. Chem. Soc.* **2011**, *133*, 17560.
- [48] Y. Zhao, L.-N. Lin, Y. Lu, S.-F. Chen, L. Dong, S.-H. Yu, *Adv. Mater.* **2010**, *22*, 5255.
- [49] C.-J. Ke, T.-Y. Su, H.-L. Chen, H.-L. Liu, W.-L. Chiang, P.-C. Chu, Y. Xia, H.-W. Sung, *Angew. Chem. Int. Ed.* **2011**, *50*, 8086.
- [50] Y. Zhu, J. Shi, W. Shen, X. Dong, J. Feng, M. Ruan, Y. Li, *Angew. Chem. Int. Ed.* **2005**, *44*, 5083.
- [51] K. M. Laginha, S. Verwoert, G. J. Charrois, T. M. Allen, *Clin. Cancer Res.* **2005**, *11*, 6944.
- [52] M. K. Yu, Y. Y. Jeong, J. Park, S. Park, J. W. Kim, J. J. Min, K. Kim, S. Jon, *Angew. Chem. Int. Ed.* **2008**, *47*, 5362.
- [53] D. J. Slamon, B. Leyland-Jones, S. Shak, H. Fuchs, V. Paton, A. Bajamonde, T. Fleming, W. Eiermann, J. Wolter, M. Pegram, J. Baselga, L. Norton, *N. Engl. J. Med.* **2001**, *344*, 783.
- [54] E. H. Romond, E. A. Perez, J. Bryant, V. J. Suman, C. E. Geyer, N. E. Davidson, E. Ta-Chiu, S. Martino, S. Paik, P. A. Kaufman, S. M. WSwain, T. M. Pisansky, L. Fehrenbacher, L. A. Lutteh, V. G. Vogel, D. W. Visscher, G. Yothers, R. B. Jenkins, A. M. Brwon, S. R. Dakhil, E. P. Mamounas, W. L. Lingle, P. M. Klein, J. N. Ingle, N. Wolmark, *N. Engl. J. Med.* **2005**, *353*, 1673.
- [55] W. Tai, R. Mahato, K. Cheng, *J. Controlled Release* **2010**, *146*, 264.
- [56] Y.-J. Bang, E. V. C. Cutsem, A. Feyereislova, H. C. Chung, L. Shen, A. Sawaki, F. Lordick, A. Ohtsu, Y. Omuro, T. Satoh, G. Aprile, E. Kulikov, J. Hill, M. Lehle, J. Rüschhoff, Y.-K. Kang, *Lancet* **2010**, *376*, 687.
- [57] W. Arap, *Science* **1998**, *279*, 377.
- [58] H. J. Lim, D. Masin, N. L. Micintosh, T. D. Madden, M. B. Bally, *J. Pharmacol. Exp. Ther.* **2000**, *292*, 337.